www.afm-journal.de

# Printing 2D Conjugated Polymer Monolayers and Their Distinct Electronic Properties

Prapti Kafle, Fengjiao Zhang, Noah B. Schorr, Kai-Yu Huang, Joaquín Rodríguez-López, and Ying Diao\*

Recently, 2D monolayer films of conjugated polymers have gained increasing attention owing to the preeminence of 2D inorganic films that exhibit unique optoelectronic and mechanical properties compared to their bulk analogs. Despite numerous efforts, crystallization of semiconducting polymers into highly ordered 2D monolayer films still remains challenging. Herein, a dynamic-template-assisted meniscus-guided coating is utilized to fabricate continuous, highly ordered 2D monolayer films of conjugated polymers over a centimeter scale with enhanced backbone  $\pi$ - $\pi$  stacking. In contrast, monolayer films printed on solid substrates confer upon the 1D fiber networks strong alkyl side-chain stacking at the expense of backbone packing. From single-layers to multilayers, the polymer  $\pi$ -stacks change from edge-on to bimodal orientation as the film thickness reaches ≈20 nm. Spectroscopic and cyclic voltammetry analysis reveals an abrupt increase in J-aggregation and absorption coefficient and a decrease in bandgap and highest occupied molecular orbital level until critical thickness, possibly arising from the straightened polymer backbone. This is corroborated by an abrupt increase in hole mobility with film thickness, reaching a maximum of 0.7 cm<sup>2</sup> V<sup>-1</sup> s<sup>-1</sup> near the critical thickness. Finally, fabrication of chemical sensors incorporating polymer films of various thicknesses is demonstrated, and an ultrahigh sensitivity of the ≈7 nm thick ultrathin film (bilayers) to 1 ppb ammonia is shown.

#### 1. Introduction

In recent years, 2D materials have made it to the forefront of materials research owing to their outstanding properties compared to bulk counterparts.<sup>[1]</sup> Reduction in dimension to atomic or molecular level thickness endows them with unique physical, chemical, optoelectronic, and mechanical properties with broad range of applications.<sup>[2]</sup> Although inorganic and carbon materials have remained the focal point in 2D materials

P. Kafle, Dr. F. Zhang, K.-Y. Huang, Prof. Y. Diao
Department of Chemical and Biomolecular Engineering
University of Illinois at Urbana-Champaign
600 South Mathews Avenue, Urbana, IL 61801, USA
E-mail: yingdiao@illinois.edu
N. B. Schorr, Prof. J. Rodríguez-López
Department of Chemistry
University of Illinois at Urbana-Champaign
505 S Mathews Avenue, Urbana, IL 61801, USA
The ORCID identification number(s) for the author(s) of this article

can be found under https://doi.org/10.1002/adfm.201909787.

DOI: 10.1002/adfm.201909787

research, their success has incentivized and laid a fertile ground for 2-dimensionalization of functional organic materials.

Recently, studies pertaining monolayer films of conjugated polymers have been surging.[3] The ability to fabricate ultrathin films of organic semiconductors (OSC) have elucidated the critical role of the first few monolayers in charge transport in fieldeffect transistors.[3h,l,4] Ultrathin films of organic semiconductors also exhibit unique properties such as uniform microstructure and constant carrier densities, compared to the thicker films.<sup>[2c,5]</sup> Moreover, ultrathin polymer films have also been shown to hold a great potential in development of highly sensitive sensors for health and environmental monitoring, by virtue of unhindered interaction of the analytes with charge carriers in the conduction channel.<sup>[3d]</sup> To that end, several solution processing methods such as Langmuir-Blodgett, [3m,o,p] Langmuir–Schaefer,[3d,f,k] dip-coating,[3a,c,l,n,6] spin-coating, [3b,e,h,j,7] bar-coating, [3g] and aged solution[3i] have been employed to fabricate monolayer films of conjugated polymers. A few of these works<sup>[3c,g]</sup> have

elucidated that formation of polymer preaggregates in solution might facilitate multilevel self-assembly process for fabrication of monolayer films. However, preaggregation inevitably results in 1D fiber networks, not true continuous 2D films. This is largely due to the 1D nature of conjugated polymer crystallization with the fastest growth axis along the polymer backbone direction.<sup>[8]</sup> We believe that high conformational degrees of freedom of the polymer chains hinders interchain interactions and therefore 2D growth. Moreover, the reported techniques may not be transferable to other systems and may not be amenable for depositing polymer films on different substrates of varying surface properties due to wetting issues. So far, a material-agnostic, substrateindependent approach for fabricating highly ordered continuous 2D monolayers does not seem to exist. Besides the fabrication challenge, fundamental questions remain; so far there are no reports on how the electronic structure (e.g., bandgap and frontier orbital energy levels) changes as the films are reduced from multilayer to monolayer.

In this work, we present dynamic-template-assisted meniscusguided coating as a new technique to fabricate 2D films of conjugated polymers over centimeter length scale within a wide processing window. This technique of 2D film fabrication is

ADVANCED FUNCTIONAL

compatible with a wide variety of substrates, as demonstrated in this work. We have shown in our previous work that using dynamic template such as ionic-liquid-infiltrated nanoporous media, conjugated polymer films printed atop exhibit high degree of alignment and crystallinity owing to strong, templatepolymer interactions and template reconfigurability.<sup>[9]</sup> In this work, we adapt this approach to fabricate 2D monolayers of two different donor-acceptor (D-A) conjugated polymers, DPP2T-TT with diketopyrrolopyrrole acceptor copolymerized with thienothiophene donor and PII-2T with isoindigo acceptor and bithiophene donor. We demonstrate enhanced 2D crystallization of conjugated polymers on dynamic template leading to highly ordered and aligned 2D monolayer films. This was in contrast to discontinuous and highly disordered monolayer films on reference solid substrates, which favored ordering of alkyl side-chains instead of polymer backbone. By systematically increasing the film thickness, we also investigated film morphology, molecular packing, electronic structure, and electronic properties variation with film thickness. We found that printed 2D monolayers exhibit distinct electronic structures not reported before. Ultimately, we fabricated organic field-effect transistors (OFETs) based chemical sensors with the DPP2T-TT films of various thicknesses and compared their sensitivities to ammonia gas, thus demonstrating increased sensitivity with decrease in thickness.

#### 2. Results and Discussion

#### 2.1. Dynamic-Template-Assisted Meniscus-Guided Printing

We employed dynamic-template-assisted meniscus-guided coating to obtain conjugated polymer films from solution

(Figure 1a). The meniscus-guided coating (MGC) is a facile technique that has been used previously to coat large area films of organic semiconductors and is adaptable to industrially compatible roll-to-roll printing.<sup>[10]</sup> In this method, microliters of semiconductor ink solution is sandwiched between a coating blade and temperature-controlled stage separated by tens to hundreds of microns, giving rise to a meniscus in the gap. Depending on the coating speed, either the blade or the viscous force translates and guides the meniscus across the substrate, leading to an evaporative assembly of polymers into thin films.<sup>[11]</sup> The film thickness, morphology and molecular packing of the film can be tuned by changing process parameters such as coating speed, substrate temperature, solution concentration, and substrate chemistry.<sup>[12]</sup>

We chose to adopt dynamic templates during MGC to enhance 2D crystallization of polymer chains. Conjugated polymers intrinsically assemble as 1D fibers. Dynamic template can assist in 2D crystallization in two ways. Firstly, strong interaction between the dynamic template and conjugated polymer can enrich the polymer concentration near the template-ink solution interface, thus facilitating the polymer self-interaction and promoting growth along the  $\pi$ - $\pi$  stacking direction. Second, the dynamic template surfaces aid in the mobility of the polymer adsorbed on the template thereby facilitating 2D growth. This is in contrast to the static substrates where enhanced interaction between the substrate and the polymer immobilizes the adsorbed polymer and hinders diffusion along the surface. Another important aspect of using dynamic-template-assisted MGC is its laxity in the choice of substrate for film transfer. Depending on the final application, it could be desirable to fabricate conjugated polymer films on different substrates. However, those substrates might not result

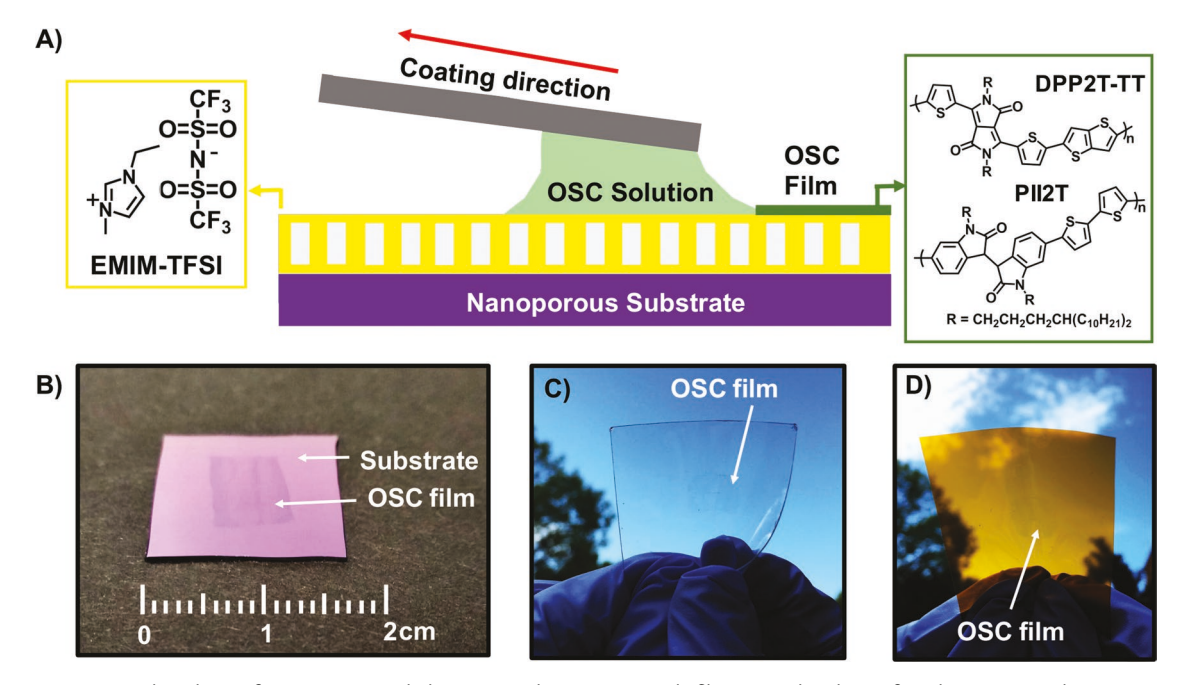


Figure 1. Dynamic template design for meniscus guided coating and centimeter scale films coated and transferred to various substrates. a) Schematic illustration of dynamic-template-assisted meniscus-guided coating setup. The dynamic template consists of an ionic liquid—EMIM-TFSI infiltrated in nanoporous matrix anodized aluminum oxide (AAO). Two donor–acceptor conjugated polymers- DPP2T-TT and PII-2T are used. 7.5 nm thick films of DPP2T-TT printed on IL and transferred to b) OTS– $SiO_2$  and flexible substrates c) PET and d) polyimide film.

www.afm-journal.de

in desired self-assembly of polymer when used as printing substrates directly. Printing of the polymer films on IL allows transfer of the films to virtually any substrate.

To incorporate the dynamic template on the MGC setup, a nanoporous matrix, anodized aluminum oxide (AAO) was infiltrated with an ionic liquid (IL), 1-ethyl-3-methylimidazolium bis(trifluoromethylsulfonyl)imide ([EMIM]-[TFSI]), such that the thin layer of IL surfacing on top of AAO can be used as the substrate during the printing process. During the short time frame of printing, the capillary force imposed by the AAO nanopores retain the IL in place and the polymer ink solution is immiscible with IL.<sup>[9]</sup> The molecular structure of the IL as well as the two D-A polymers used in this study- DPP2T-TT and PII-2T are shown in Figure 1. We chose imidazoliumbased IL as our previous study has shown strong interactions between the IL and polymer backbone via molecular dynamics and NMR.[9] The ink solution of DPP2T-TT and PII-2T was prepared in chloroform and chlorobenzene, respectively. The printing speed and solution concentration were varied as described in subsequent sections. The polymer films printed on the IL were transferred to octadecyltrichlorosilane (OTS) functionalized SiO2 for further characterizations (see the Experimental Section for the transfer process).

Figure 1b shows ultrathin films (thickness ≈7.5 nm) of DPP2T-TT printed on IL/AAO ensemble using 1 mg mL<sup>-1</sup> solution concentration at 0.5 mm s<sup>-1</sup> printing speed and transferred to OTS-SiO2. We also demonstrate successful transfer of the IL templated DPP2T-TT films printed at the same conditions onto two flexible substrates: polyethylene terephthalate (PET) and poly(4,4'-oxydiphenylene-pyromellitimide) films, shown in Figure 1c,d, respectively. We note that larger films can be printed when employing larger AAO to construct the dynamic template. In addition to IL, we also fabricated films of the aforementioned conjugated polymers using MGC directly on solid substrates of varying surface energies. We noticed that monolayer films could not be fabricated on surfaces with low surface energies ( $\gamma$ ) such as OTS ( $\gamma = 20.5 \times 10^{-3} \text{ N m}^{-1}$ ) because of dewetting of ink solution. Therefore, we chose substrates with higher surface energies as reference static substrates—plasma treated ( $\gamma = 67.2 \times 10^{-3} \text{ m m}^{-1}$ )[13] and phenyltrichlorosilane (PTS) ( $\gamma = 36.0 \times 10^{-3} \text{ N m}^{-1}$ )[13] functionalized SiO<sub>2</sub> (Figure S1, Supporting Information). We note that the surface energy of the IL used is comparable ( $\gamma = 36.2 \times 10^{-3} \text{ N m}^{-1}$ )<sup>[9]</sup> to that of PTS and thus rule out the effect of surface energy when comparing polymer films coated on IL versus PTS.

# 2.2. Processing Window for DPP2T-TT 2D Monolayer Fabrication

In order to find the printing conditions to fabricate 2D monolayer films of DPP2T-TT using dynamic-template-assisted MGC, we explored a wide range of solution concentrations and printing speeds and demonstrated that dynamic-template-assisted MGC can guide assembly of 2D monolayers over a wide processing window. The morphology phase diagram with solution concentrations ranging from 0.25 to 5 mg mL<sup>-1</sup> and printing speeds ranging from 0.25 to 5 mm s<sup>-1</sup> is shown in **Figure 2** indicating three distinct regimes: 2D monolayer, multilayer

and sub-monolayer. The measured thickness of 2D monolayer films on IL, 2.9–3.5 nm, is higher than the out-of-plane lamella stacking distance (≈2.48 nm) observed through grazing incidence X-ray diffraction (GIXD) of thicker DPP2T-TT films (discussed later; see **Figure 3c**,d). However, this thickness is close to the end-to-end distance between the stretched alkyl side-chain ends in DPP2T-TT monomer (≈3.7 nm) determined through a molecule visualizing software, Mercury<sup>[14]</sup> (Figure S2, Supporting Information). This suggests an edge-on oriented polymer backbone in monolayer films with possible interdigitation between side-chains of adjacent layers in multilayer films.

The morphology phase space we obtained can be rationalized and predicted by the mass balance model describing the evaporation regime of MGC. Previous work by Le Berre et al.[15] detailed a solution coating model where film deposition can be distinguished into two regimes, with distinct dependence of film thickness on coating speed. In the evaporation regime where solvent evaporation outcompetes viscous drag-out, film thickness decreases with increase in printing speed. In the Landau-Levich regime where viscous drag-out dominates over solvent evaporation, film thickness increases with increasing printing speed. For 5 mg mL<sup>-1</sup> DPP2T-TT/chloroform solution coated on IL at 25 °C, we have previously determined that the transition from evaporation regime to Landau-Levich regime occurs at ≈10 mm s<sup>-1</sup>.<sup>[9]</sup> With decrease in solution concentration, the viscosity of the solution decreases, hence we expect the transition speed to increase at lower solution concentration.[16] This means that for all conditions used in our study, the film deposition occurs in the evaporation regime. Indeed, we observed decrease in film thickness with increase in printing speed, and when the film thickness reached monolayer, we then observed decrease in film coverage ( $\Theta$ ) with increase in printing speed.

In the evaporation regime, satisfying the mass balance at the meniscus leads to the following equation (Equation (1))

$$h = \frac{c}{\rho} \frac{Q_{\text{evap}}}{L} \vartheta^{-1} \tag{1}$$

where h is film thickness, c is solution concentration,  $Q_{\text{evap}}$  is solvent evaporation rate, L is width of the meniscus perpendicular to printing,  $\rho$  is polymer film density, and  $\vartheta$  is the coating speed.<sup>[15]</sup> We note that the derivation of the equation assumes full coverage. For a constant film thickness with full coverage, the solution concentration required is proportional to the coating speed. Using this relationship, 2D monolayer films of DPP2T-TT was fabricated using printing conditions along the diagonal (enclosed by the black dashed line) in the phase diagram; the black dotted points in this region denote the following solution concentration (mg mL<sup>-1</sup>)/printing speed (mm  $s^{-1}$ ), respectively: 0.25/0.25, 0.5/0.5/ 2.5/2.5, and 5/5 (Figure S3, Supporting Information). We rationalize that at these conditions, the flux of polymer mass determined by both solvent evaporation and the solution concentration is just enough for covering monolayer film and not enough to grow upper layers. Interestingly, in all of the conditions, we observed smooth 2D films of monolayer with  $\Theta = 1$ . Moreover, at a particular solution concentration, variation of printing speed by ±0.2 mm s<sup>-1</sup> relative to the optimized conditions calculated

www.afm-journal.de

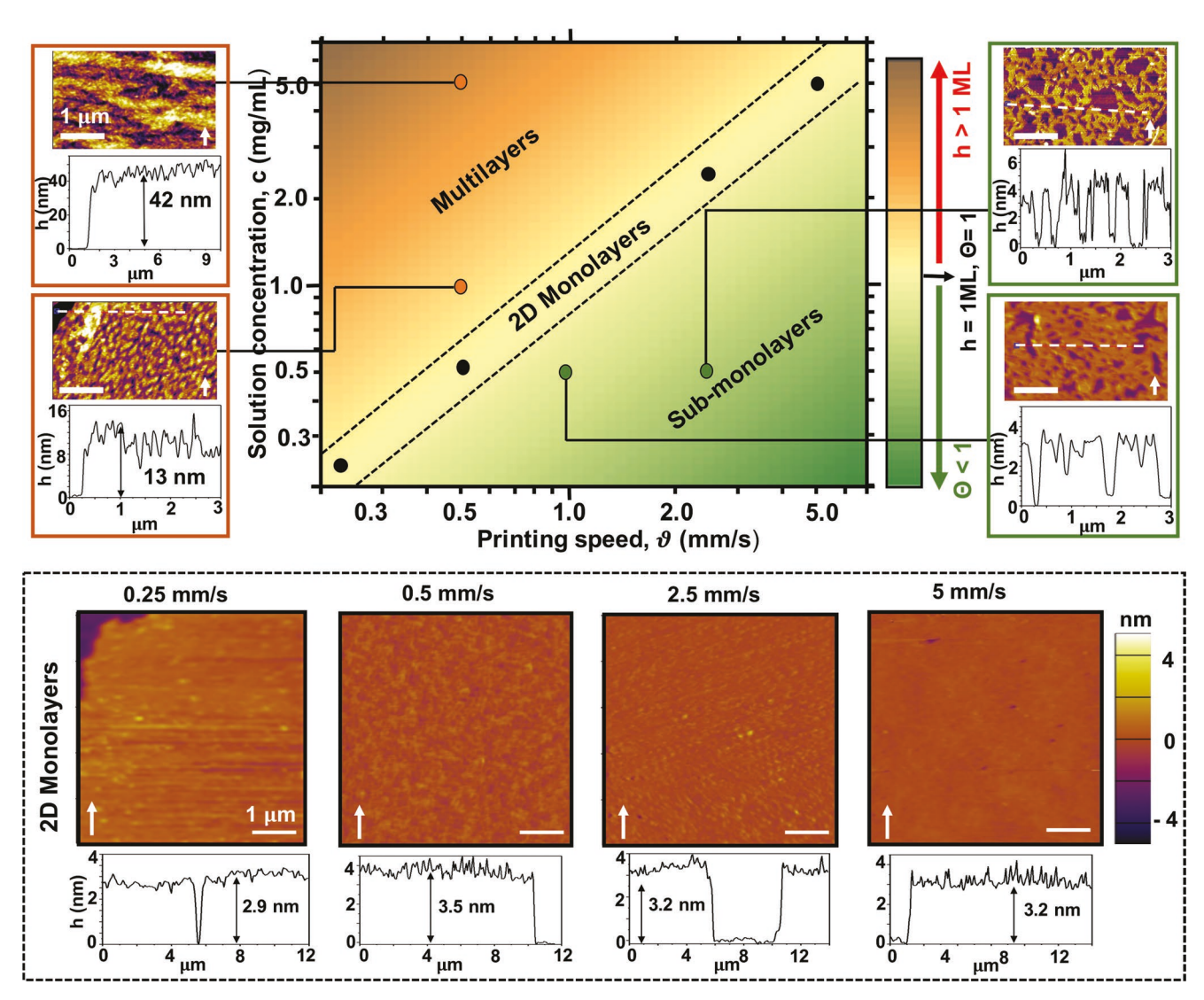


Figure 2. Morphology phase space and processing window for dynamic-template-assisted meniscus-guided coating of 2D monolayers of DPP2T-TT. Solution concentration versus printing speed plot of DPP2T-TT films on IL showing processing conditions for 2D monolayer film fabrication and thickness dependence on the process parameters. The black dots enclosed between two dotted lines represent conditions for printing 2D monolayer films, whose respective AFM images and height profiles are shown below the plot. The films printed at 0.25, 0.5, 2.5, and 5 mm s<sup>-1</sup> used solution of concentration 0.25, 0.5, 2.5, and 5 mg mL<sup>-1</sup>, respectively. When solution concentration was increased or printing speed was decreased beyond the conditions inside the dashed lines, multilayer films are obtained (two examples indicated by orange dots). In contrast, when solution concentration was decreased or the printing speed was increased, the films were sub-monolayers with coverage ( $\Theta$ ) less than 1 (two examples indicated by green dots). The white arrows in the AFM images indicate coating direction.

still resulted in monolayer films with full coverage, indicating that 2D monolayer fabrication is tolerant to small perturbations in coating conditions. The molecular packing of monolayer films printed under all conditions exhibited similar packing (described in detail in section below) except the one at 5 mm s $^{-1}$  which did not show any  $\pi$ – $\pi$  stacking peak (Figure S4, Supporting Information). For further characterization of monolayer films printed in IL, we chose 0.5 mg mL $^{-1}$  solution concentration and 0.5 mm s $^{-1}$  printing speed.

As we diverge from the diagonal in the phase diagram by either changing the solution concentration or printing speed, we enter the multilayer or the sub-monolayer regime. Increasing concentration and/or lowering printing speed from the diagonal

2D monolayer region resulted in multilayer films with no pinholes. With those variations in printing conditions, the inflow of the polymer must have been greater than what is required for full monolayer coverage. In contrast, increasing printing speed and/or decreasing solution concentration decreased the polymer mass at the contact line during solvent evaporation resulting in sub-monolayers with  $\Theta$  < 1 and fractal dimension <2.

To test the uniformity of the monolayer films printed using dynamic template MGC, we took AFM images of various regions in a single monolayer film of DPP2T-TT printed using 0.5 mg mL $^{-1}$  solution at 0.5 mm s $^{-1}$ . Figure S5 (Supporting Information) shows highly uniform continuous 2D monolayer film of DPP2T-TT over centimeter scale area.

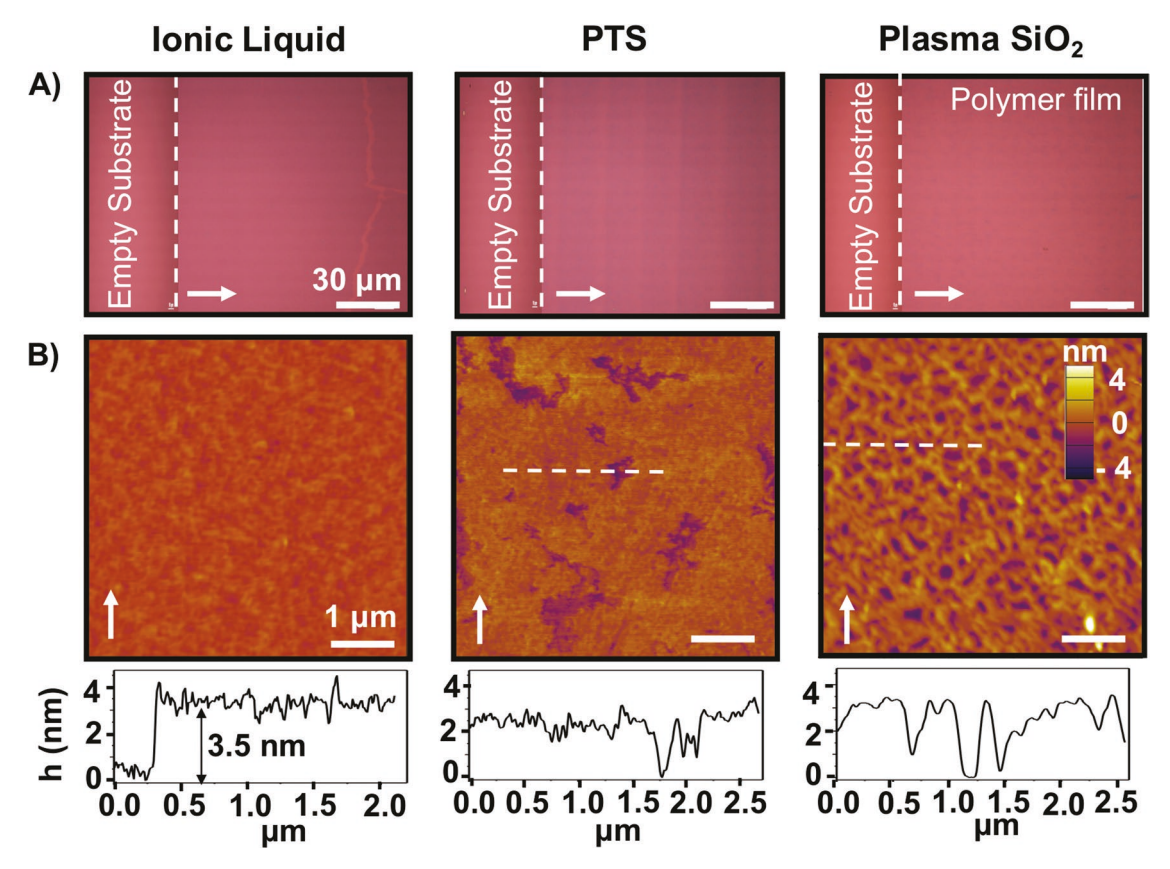


Figure 3. Optical microscopy images and AFM micrographs of DPP2T-TT monolayer films coated on three different substrates. a) Optical microscopy images of DPP2T-TT films printed on IL, PTS, and plasma treated  $SiO_2$ . The section of the image to the left of white dotted lines are empty substrates and that to the right are monolayer polymer films. b) Tapping-mode AFM height images of DPP2T-TT monolayer films printed the three substrates accompanied with the height profile (shown by white dotted lines on AFM images in the case of PTS and plasma  $SiO_2$ ). The white arrows in all of the images indicate coating direction.

# 2.3. Morphology and Molecular Order in DPP2T-TT 2D Monolayers

Next, we characterized the morphology and molecular packing in 2D monolayer films coated on IL and transferred to OTS functionalized SiO<sub>2</sub>, in comparison to those coated on reference substrates. Figure 3a shows optical microscopy images of monolayer on IL and reference solid substrates prepared from 0.5 mg mL<sup>-1</sup> chloroform solution and a printing speed of 0.5 mm s<sup>-1</sup>. While the monolayer film printed on IL is uniform, those on reference substrates appear inhomogeneous. Moreover, the monolayer film printed on PTS suffers from stick-and-slip meniscus instability<sup>[17]</sup> that usually appears on low-surface-energy substrates. Despite having comparable surface energies, IL dynamic template suppressed such stick-and-stick phenomenon as meniscus-pinning does not occur on liquid surfaces.

We then employed atomic force microscopy (AFM) to unveil the mesoscale morphology of the monolayer films on all substrates (Figure 3b). In contrast to the IL printed films which was observed to be smooth and continuous without any voids, the optimized monolayer films on plasma treated  $\rm SiO_2$  (at 0.5 mm s<sup>-1</sup>) consisted of fiber-network-like morphology with a coverage of only 69%. In fact, 2D monolayer could not be obtained at any printing speed attempted (0.1–100 mm s<sup>-1</sup>

at 0.5 mg mL<sup>-1</sup>) (Figure S6, Supporting Information). While the low surface energy of the PTS might have lowered the Gibbs' free energy for nucleation on PTS substrates compared to plasma treated SiO<sub>2</sub>, [13] the monolayer film was still riddled with voids, giving a film coverage of ≈86%. Quantitatively, we determined using an image analysis protocol we developed [18] that the fractal dimension of the monolayer films on IL is 2, which significantly decreases to  $1.33 \pm 0.06$  and  $1.48 \pm 0.05$  for those on plasma SiO<sub>2</sub> and PTS, respectively.

To investigate molecular packing of polymer chains, we employed GIXD on monolayer films. Interestingly, a strong peak at  $q_{xy} = 1.74 \text{ Å}^{-1}$  was observed in monolayer films on IL when scanned with incidence X-ray perpendicular to the printing direction (Figure 4a and Figure S7, Supporting Information). This peak informs an in-plane  $\pi$ - $\pi$  stacking distance of 3.6 Å and that the polymer backbones adopt an "edge-on" orientation in the crystalline domains. This peak was almost absent when the film was oriented parallel to printing. This suggests a high degree of alignment of the polymer backbone oriented perpendicular to printing (Figure 4b-i). Taking the ratio of the in-plane  $\pi$ - $\pi$  stacking peak intensities in perpendicular to parallel directions gave a high dichroic ratio of 5.6 (Figure 4c). We note that the faint, aperiodic out-of-plane peaks along qz arise from superimposed form factors of crystalline OTS and the polymer monolayer (Figure S8, Supporting

www.afm-journal.de

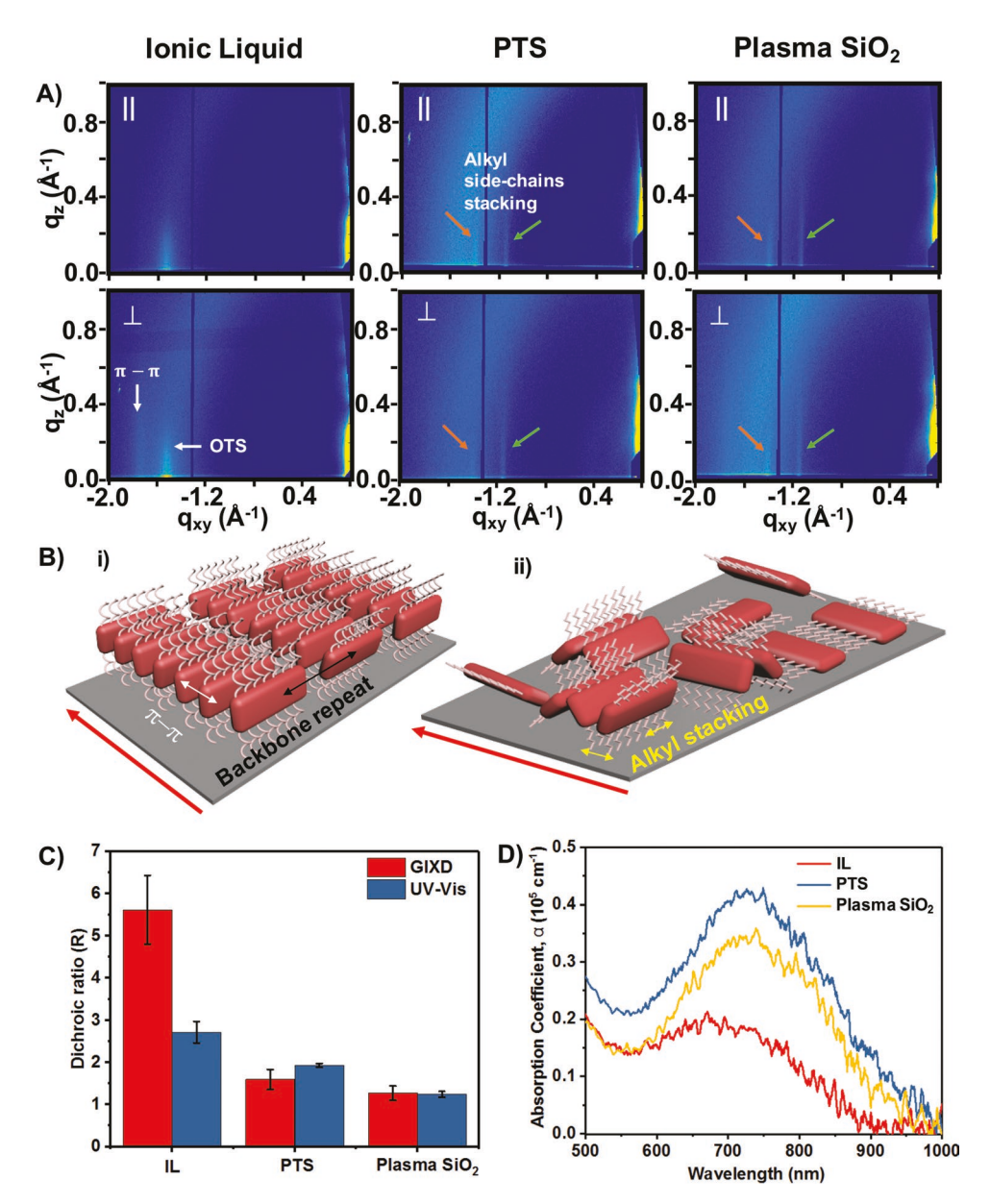


**Figure 4.** Comparison of molecular packing, polymer chain alignment, and polymer conformation in monolayer films printed on IL and reference substrates. a) Grazing incidence X-ray diffraction (GIXD) images of DPP2T-TT monolayer films printed on the three substrates with incident beam parallel (top) and perpendicular (bottom) to the coating direction. The white dotted box arrow points  $\pi$ – $\pi$  stacking peak between polymer backbone. The green and orange arrows point two peaks at  $q_{xy} = 1.14$  and 1.40 Å<sup>-1</sup>, respectively. These peaks possibly arise alkyl side-chains stacking. The strong out-of-plane peaks indicate lamella stacking perpendicular to the substrate. The strong peak at  $q_{xy} \approx 1.5$  Å<sup>-1</sup> is due to OTS. b) Molecular stacking model of DPP2T-TT printed on i) Ionic liquid ii) PTS and plasma treated SiO<sub>2</sub>. c) UV–vis and GIXD dichroic ratios of DPP2T-TT monolayer films coated on different substrates. d) Absorption coefficient (α) of monolayer film on IL and reference substrates.

Information);<sup>[19]</sup> the absence of out-of-plane lamella peaks in these films further validate that the films printed are monolayer. In contrast, the GIXD spectra of monolayer films on reference substrates were strikingly different from those on IL. No  $\pi$ – $\pi$  stacking peak was observed in either of the reference substrates, instead two strong peaks at  $q_{xy}\approx 1.14$  and 1.40 Å<sup>-1</sup> appeared in both parallel and perpendicular direction relative to the printing direction. We attribute the peak at 1.40 Å<sup>-1</sup> to alkyl side-chains stacking.<sup>[20]</sup> This suggests that while IL induces ordering of the backbone, reference substrates promote alkyl

side-chains stacking at the cost of backbone packing along  $\pi$ – $\pi$  stacking direction (Figure 4b-i,ii). We observed that the peak at 1.14 Å<sup>-1</sup> appears at the exact same location for both DPP2T-TT and PII-2T (discussed in detail later) printed on reference substrates, which have distinct backbone structures but the same alkyl side-chains. In addition, the peak at 1.14 Å<sup>-1</sup> always appears together with the peak at 1.40 Å<sup>-1</sup>. Hence, we believe that both peaks emerge from alkyl side-chains stacking. The alignment of the polymer chains was also poor on the solid substrates with GIXD dichroic ratio of only 1.60 and 1.27 on

ADVANCED FUNCTIONAL MATERIALS

PTS and plasma SiO<sub>2</sub>, respectively, determined using the intensities of the peak at  $q_{xv} \approx 1.14$ .

Next, we employed polarized UV-vis spectroscopy to compare the degree of global alignment of crystalline and amorphous region in DPP2T-TT monolayers printed on different substrates. We expect maximum absorption when the transition dipole moments align with the polarizer axis, thus the degree of alignment of the polymer backbone can be quantified using the dichroic ratio,  $R = I_{\perp}/I_{\parallel}$  of the UV-vis peaks where  $I_{\perp}$  and  $I_{\parallel}$  denote the absorbance when printing direction is perpendicular and parallel to the polarizer. The largest component of the transition dipole of DPP2T-TT is expected to be parallel to the polymer backbone. Indeed, we observed maximum absorbance for monolayers printed in IL when coating direction was positioned perpendicular to the polarizer with a dichroic ratio of 2.7 (Figure 4b and Figure S9, Supporting Information) determined using the peak at ≈700 nm. In contrast, the dichroic ratio of monolayers on PTS and plasma treated SiO2 were lower (1.9 and 1.2, respectively), indicating reduced backbone alignment.

Next to probe into the conjugation length of the polymer chains in monolayer films, we determined the absorption coefficient,  $\alpha$ , by averaging the absorption spectra of each film over multiple in-plane rotation angles. Interestingly, the monolayer films on IL had the lowest value of  $\alpha$ , almost 2.3 and 1.7 times lower than that of PTS and plasma SiO<sub>2</sub>, respectively (Figure 4d). The decrease in  $\alpha$  may be attributed to the decrease in conjugation length of the polymer which could ensue because of decreasing backbone planarity.<sup>[21]</sup> Moreover, the peak at  $\approx$ 700 also seems to be blue-shifted for IL printed monolayer by roughly 20–40 nm. Both of these spectral observations corroborate and further validate that the polymer backbone has decreased planarity in monolayer films on IL compared to reference substrates.

The observed morphological and molecular packing differences of monolayer DPP2T-TT films clearly indicate distinct growth modes of polymer on dynamic versus static substrates. While the monolayer films on reference substrates consisted of fiber-network-like morphology riddled with voids, those printed on IL was 2D, smooth, continuous, and void-free. These distinct morphology characteristics validate our hypothesis that IL indeed promotes 2D crystallization of the polymer films with backbone alignment. However, enhanced backbone crystallization seems to be at the expense of reduced backbone planarity.

# 2.4. Thickness Dependent Morphology and Molecular Packing

Next, we compare DPP2T-TT monolayers with thicker films in terms of the morphology and molecular packing and determine how these parameters evolve with film thickness. We first focus our discussion on IL-templated films and then validate the trend using reference substrates. We systematically increased the film thickness from  $3.5 \pm 0.5$  nm (monolayer) to  $42.3 \pm 3.7$  nm by increasing solution concentration from 0.5 to 5 mg mL<sup>-1</sup>, while keeping the printing speed constant at 0.5 mm s<sup>-1</sup>. **Figure 5a** shows linear relationship ( $R^2 = 0.998$ ) between the solution concentration used and the resulting film thickness as expected from Equation (1). The polarized optical microscopy images of DPP2T-TT films (Figure S10, Supporting Information) show

that the birefringence increases with thickness until ≈27 nm, but decreases with further increase in thickness. This suggests a non-monotonic dependence of in-plane alignment with film thickness. The AFM images of the polymer films also exhibited pronounced differences with increasing film thickness (Figure 5b). In monolayer (3.5  $\pm$  0.5 nm) and 7.5  $\pm$  1.3 nm thick film, the morphology appeared smooth with root mean square roughness of around 0.32 and 0.45 nm, respectively. However, when the film thickness reaches around 14 nm, islands of the polymer domains of about 200 nm diameter and ≈7 nm thick appear on film surface. With further increase in film thickness to ≈42 nm, large fiber-like domains reaching several hundreds of nanometer wide and microns long are observed. The stark contrast in film morphology between monolayers and thicker films suggests a distinct growth mechanism of monolayers on IL that promotes 2D growth.

We further studied and compared the molecular packing of DPP2T-TT in monolayer and thicker films. As described in earlier sections, the GIXD pattern of monolayer film only exhibited  $\pi - \pi$  stacking peak in the  $q_{xy}$  direction, indicating highly edge-on orientation of crystalline domains. Further, no lamella stacking peak was observed along the  $q_z$  direction. Instead, the scattering features originate from form factors of DPP2T-TT and OTS superimposed. From monolayer to multilayers, distinct lamella stacking peak appeared and the edge-on  $\pi$ - $\pi$  stacking peak increased in intensity in the perpendicular direction (Figure 5c,d-i). The  $\pi$ - $\pi$  stacking peak intensity remained low in the parallel direction (Figure S11, Supporting Information), indicating that the high degree of in-plane alignment was retained, with dichroic ratio of 5.6 in monolayer and reaches as high as ≈23 in 20 nm thick film. Interestingly, below 20 nm DPP2T-TT films, we only observed in-plane, edge-on  $\pi$ - $\pi$  stacking peaks; when the film thickness reached 20 nm, an out-of-plane, face-on  $\pi$ - $\pi$ stacking peak also emerged. This indicates that the  $\pi$ -stacks evolved from edge-on to bimodal from monolayers to 20 nm. This may be attributed to stochastic nucleation in the bulk solution or solution-air interface that competes with nucleation templated by IL surface, when solution concentration is increased. For films printed on the two references substrates, we observe the edge-on stacking peak appear starting from ultrathin films (7-10 nm) but not in monolayers. Similarly, the change of polymer orientation from edge-on to bimodal was also observed starting from 20 to 25 nm thick film (Figures S12–S15, Supporting Information).

### 2.5. Thickness Dependent Electronic Structure

After establishing the distinct morphology and molecular packing in 2D monolayers of DPP2T-TT from that of multilayers, we probed into the electronic structure of monolayers as compared to multilayers employing UV–vis spectroscopy and cyclic voltammetry (CV). Figure S16 (Supporting Information) shows the UV–vis spectra of DPP2T-TT films of various thicknesses printed on IL and transferred to OTS-functionalized glass substrates. The spectra reveal two distinct absorption peaks at  $\approx 830$  and  $\approx 730$  nm with the higher and lower wavelength peaks indicating the lowest energy electronic transition

www.advancedsciencenews.com www.afm-journal.de

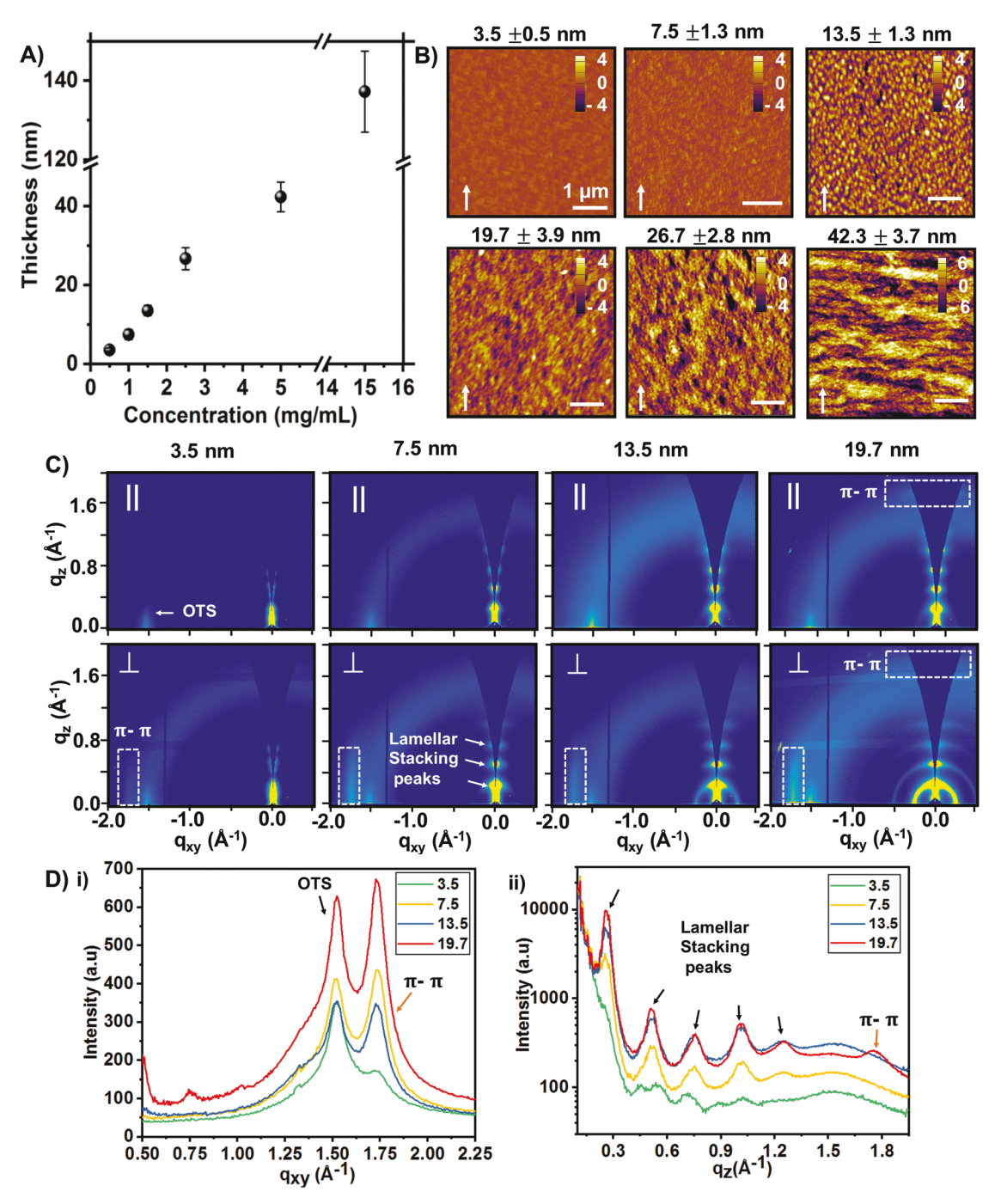


Figure 5. Thickness dependent morphology and molecular stacking in DPP2T-TT films. a) Thickness versus concentration plot of DPP2T-TT films printed on IL at 0.5 mm s<sup>-1</sup> coating speed and 25 °C stage temperature. b) Tapping-mode AFM height images of DPP2T-TT films of varying thicknesses. The white arrows indicate the coating direction c) GIXD images of DPP2T-TT monolayer and thicker films printed on IL with the incident beam parallel (top) and perpendicular (bottom) to the coating direction. The white dotted line highlights the  $\pi$ - $\pi$  stacking peak. d) 1D-GIXD intensity curves of IL printed DPP2T-TT films of different thickness. The curves are obtained by azimuthal integration of radial slices of 2D GIXD images shown in (c) with azimuthal angles i) –88° to –83° (in-plane, parallel, and perpendicular to the coating direction) and ii) –14° to –9° (out-of-plane).

or 0–0, and higher energy vibrionic replica 0–1, respectively. The positions and relative intensities of 0–0 and 0–1 peaks can be employed as spectral signatures to comprehend the internal electronic structure of the polymer assemblies in solution or solid thin films.<sup>[21,22]</sup>

To directly compare the electronic structure, we first normalized the UV-vis spectra by the intensity of the 0-1 peak for all thicknesses. Interestingly, the normalized spectrum of the monolayer DPP2T-TT film looks unusually different from that of thicker films with much lower 0-0/0-1 peak intensity ratio

www.afm-journal.de

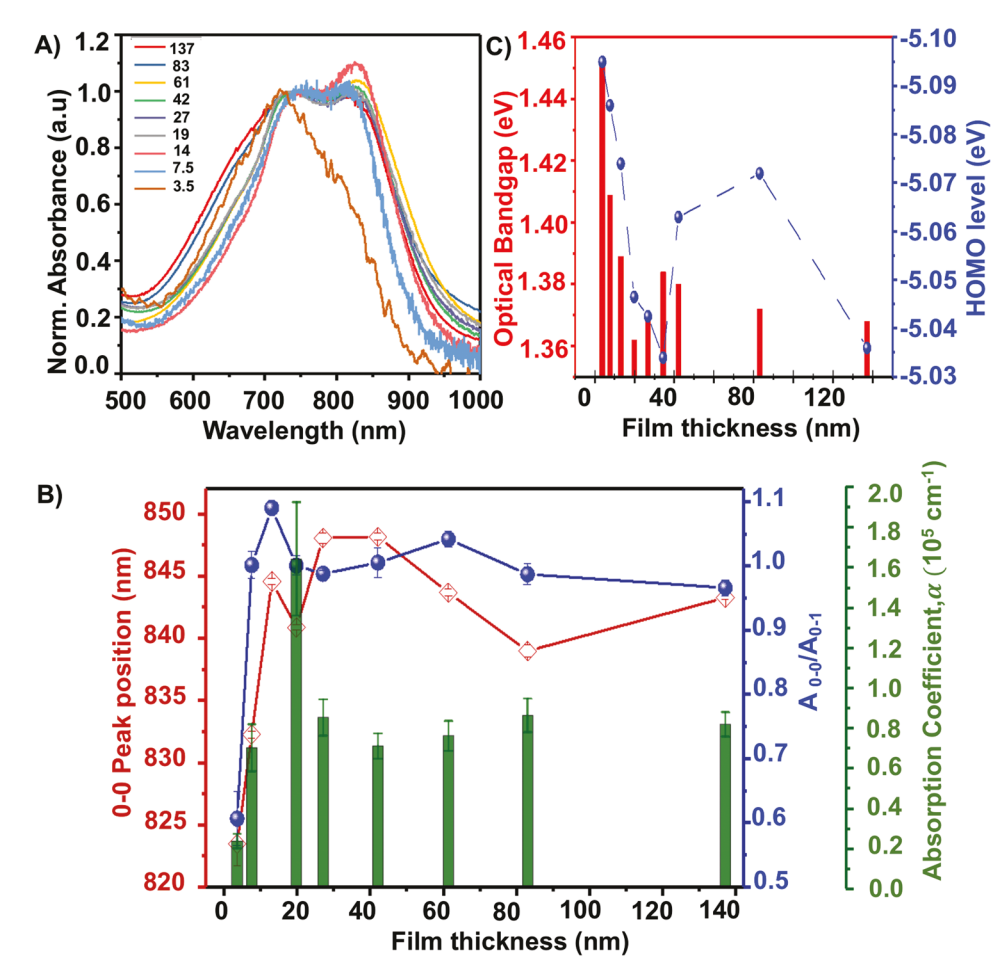


Figure 6. Determining thickness dependent electronic structure of DPP2T-TT films printed on IL. a) UV–vis spectrum of DPP2T-TT films of varying thickness (nm) printed on IL, transferred to OTS-glass, normalized with respect to the 0–1 vibrionic peak. b) Peak position of 0-0 vibrionic peak, intensity ratio of 0–0 and 0–1 peaks  $(A_{0-0}/A_{0-1})$  and absorption coefficient,  $\alpha$  of DPP2T-TT films, with varying thickness of DPP2T-TT printed on IL. c) Optical bandgap and HOMO energy level of DPP2T-TT films on IL obtained via UV–vis and CV, respectively.

 $(A_{0-0}/A_{0-1})$  than even the 7.5 nm film (**Figure 6**a). In polymer assemblies, higher  $A_{0-0}/A_{0-1}$  is associated with enhanced J-coupling or improved through-bond coupling between the head-to-tail arranged transition dipole moments (TDMs) of the monomer units.<sup>[22a,23]</sup> For a particular polymer with same number of repeat units, this enhancement in the J-coupling or its observable  $A_{0-0}/A_{0-1}$ , could signify improved planarity of the polymer chain. [22b,24] In contrast, coupling between chromophoric units that belong to different polymer chains and lie side-by-side gives rise to H-coupling. The resulting changes in spectral signatures due to H-aggregation compared to isolated polymer chains is diametrically opposed to I-coupling, i.e.,  $A_{0-0}/A_{0-1}$  decreases with enhanced H-coupling.<sup>[22a,23]</sup> We observed that the  $A_{0-0}/A_{0-1}$  value increases by almost 65% from 0.61 in monolayer to 1.00 in 7.5 nm film, reaches the highest value of 1.09 at ≈14 nm and gradually decreases on further thickness increase (Figure 6b). This suggests the distinct electronic structure of monolayers from even the bi- or trilayer film and that the intrachain interaction is drastically enhanced from monolayer to multilayers. We also observed that the 0-0 vibrionic peak is significantly blue shifted in monolayer compared to thicker films. Alike the trend of  $A_{0-0}/A_{0-1}$ 

with film thickness, the 0-0 electronic transition seems to undergo bathochromic shift as thickness is increased until it plateaus at ≈27 nm and then undergoes a slight hypsochromic shift with further thickness increase. This trend is consistent with our inference that J-aggregation or the planarity of the polymer backbone is enhanced from monolayer to multilayer, which peaks at ≈14 nm. To further validate this point, we determined the absorption coefficient,  $\alpha$ , of thicker films. Interestingly, the monolayer film had lowest  $\alpha$  value which dramatically rises by sevenfolds with film thickness increase to 20 nm; further increase in thickness results in declination of its value (Figure 6b). While change in out-of-plane orientation distribution of polymer backbones could alter  $\alpha$  value, we emphasize that the polymer films below 20 nm all exhibit comparable backbone orientation with the transition dipole parallel to the substrate plane and yet  $\alpha$  values were modulated drastically from monolayer to 20 nm film. The increase in  $\alpha$  also corroborates with our observation from other spectral signatures that the backbone planarizes when thickness is increased from monolayer up to a critical thickness. We also point out that obtaining accurate  $\alpha$  requires 3D isotropic films; the values obtained from 2D films (i.e., with in-plane TDM only) could be



www.afm-iournal.de

overestimated by about 50%. However, such a drastic increase in  $\alpha$  from monolayer to 20 nm film observed in DPP2T-TT is significantly larger than the possible error.

Next, we investigated the frontier energy levels and bandgap variation of DPP2T-TT with film thickness given their crucial roles in charge injection and transport. For this, we obtained optical bandgap from the UV-vis spectra through Tauc-plot (Figure 6c). Consistent with the above inference, monolayer films exhibited the highest bandgap of 1.45 eV, which markedly decreased with increase in film thickness reaching a lowest 1.36 eV in 20 nm films; further increase in film thickness resulted in slight increase in its value. We attribute the initial drop in bandgap from monolayer to thicker films to enhanced J-aggregation due to increased conjugation. [25] We further gauged the contribution of frontier energy level changes to the bandgap variation. The highest occupied molecular orbital (HOMO) was calculated from the onset of oxidation potential from CV (Figure S17, Supporting Information) and the lowest unoccupied molecular orbital (LUMO) energy level was determined from HOMO energy level and optical bandgap calculated previously. Much like the trend observed in bandgap, the HOMO levels of the film also lowers (becomes less negative) from monolayer (-5.10 eV) until ≈34 nm (–5.03 eV), although the degree of HOMO level change is less than the extent of bandgap variation. We calculated that the planarization of the twisted backbone conformation altered both HOMO and LUMO energy levels to similar extent, both combined lowered the bandgap (Figure S18, Supporting Information). The trend in bandgap and energy level modulation with film thickness corroborates the trend inferred from UV-vis measurements. Both point to a unified picture that the twisted backbone in monolayers becomes planarized in multilayers, and that a critical thickness exists between 20 and 27 nm when the backbone is the most planar.

Furthermore, we compared the thickness dependence of DPP2T-TT films printed on IL with those printed on reference substrates, namely plasma treated SiO2 and PTS. Interestingly, we observed similar trends of enhanced backbone planarity from monolayer to thicker films printed on reference substrates. This suggests that the observed phenomenon of backbone planarization with increasing film thickness is independent of the substrate used (Figures S19-S22, Supporting Information). We note that throughout the thickness range investigated, the film deposition occurs in evaporation regime. Hence we speculate that, in this case, the planarization of the backbone at a critical thickness range seems to occur not because of change in flow regimes, but rather due to combined effect of reduced influence of substrate-induced crystallization as film thickness increases as well as increased bulk and top surface nucleation as solution concentration is increased.

#### 2.6. Charge Transport Properties of DPP2T-TT Films

To characterize the substrate- and thickness-dependent charge transport properties of DPP2T-TT films and to establish the structure–property relationship, we fabricated field-effect transistors of top-contact bottom-gate (TCBG) configuration. For this purpose, we used highly n-doped Si and 300 nm  $\rm SiO_2$  layer as gate and dielectric, respectively. For the reference substrates, polymer films were directly printed on plasma treated or PTS

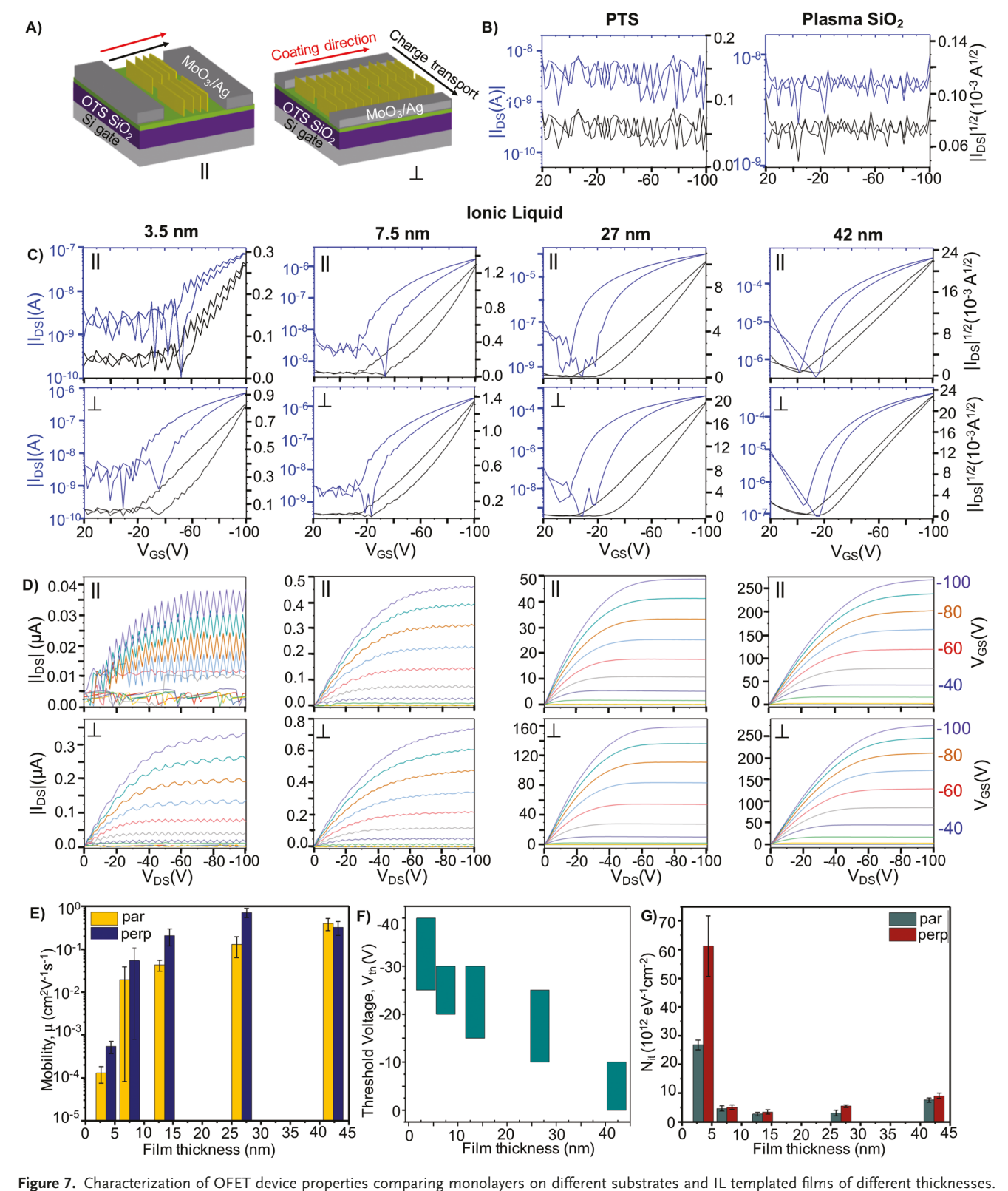
Surprisingly, we observed that the monolayer films fabricated on plasma treated SiO2 and PTS did not show any charge transport property (Figure 7b) despite that the film provides continuous pathways for charge carriers (Figure 3a). The absence of  $\pi$ - $\pi$  stacking, low degrees of alignment, low fractal dimension together with twisted conformation of the backbone could have significantly obstructed charge carrier pathway in films templated by reference substrates. Figure 7c,d show the transfer and output curves of the best performing devices with various thicknesses of DPP2T-TT films printed on IL. Unlike the reference films, IL-templated monolayers exhibited measurable charge transport properties in both parallel and perpendicular direction to printing, albeit with a very low on-current and consequently high noise. We attribute this improvement from reference films to enhanced intra- and intermolecular ordering, high degree of alignment and increased coverage/ fractal dimension. We also compared the hole mobility in three different regions of monolayer films which are least affected by film transfer process and observed fairly uniform mobility in both parallel and perpendicular to coating direction (Figure S23, Supporting Information). Addition of more layers drastically improved the charge transport properties reaching near-ideal transfer and output curves. Interestingly, addition of just one molecular layer to the monolayer film increased the mobility by more than 2 orders of magnitude in both parallel and perpendicular directions. The mobility along both directions increased monotonically until reaching ≈27 nm of film thickness where the average mobility in perpendicular and parallel direction was ≈0.73 and 0.13 cm<sup>2</sup> V<sup>-1</sup> s<sup>-1</sup>, respectively (Figure 7e). Generally, the mobility was higher along perpendicular direction (along the polymer backbone) with the highest anisotropy  $(\frac{\mu_{\text{perp}}}{\mu_{\text{max}}} = 5.6)$  achieved at the critical thickness of  $\approx 27$  nm. Further increasing the film thickness decreased the mobility anisotropy to almost unity at 42 nm, corroborating with a loss of alignment in films also observed in polarized optical microscopy images (Figure S10, Supporting Information). Besides sharp change of mobility with film thickness, the threshold voltage  $(V_{th})$  was strikingly shifted from -40--30 to -10-0 V from monolayers to multilayers. Such a drastic change in  $V_{th}$  cannot be fully explained by the slight HOMO level shift (Figure 7f). To rationalize the thickness dependence of mobility and threshold voltage, we calculated interfacial trap state density  $(N_{it})$  from the subthreshold swing using the following equation (Equation (2))

$$N_{it} = C_{ox} \left( S \times e / (k_B T \ln 10) - 1 \right) / e^2$$
 (2)

where  $C_{ox}$  is the capacitance per unit area of the dielectric, S is the subthreshold swing, e is the elementary charge,

www.advancedsciencenews.com www.afm-journal.de





a) Schematic illustration of OPET device properties comparing monolayers on different substrates and it templated films of different thicknesses. a) Schematic illustration of top-contact bottom-gate OPET devices of DPP2T-TT films to determine charge transport properties in parallel and perpendicular direction to printing. b) Transfer curves of DPP2T-TT monolayer films printed on PTS and plasma treated SiO<sub>2</sub>. c)Transfer and d) output curves of IL templated DPP2T-TT films of various thicknesses determined parallel (top) and perpendicular (bottom) to the coating direction. e) Hole mobility, f) threshold voltage ( $V_{GS}$ ) variation of DPP2T-TT films with film thickness, and g) interfacial trap state density ( $N_{it}$ ). The source—drain voltage ( $V_{DS}$ ) used in all cases is -100 V. The histogram of hole-mobility in monolayer and thicker films along parallel and perpendicular direction is shown in Figure S24 (Supporting Information).

Adv. Funct. Mater. 2020, 1909787

www.afm-journal.de

 $k_{\rm B}$  is the Boltzmann's constant, and T is the absolute temperature. [26] We noticed that  $N_{\rm it}$  for monolayer is  $27 \times 10^{12}$  and  $62 \times 10^{12} \text{ eV}^{-1} \text{ cm}^{-2}$  along parallel and perpendicular directions, respectively, which is almost 6 and 12 times larger than  $N_{it}$ in 7.5 nm thick films in the respective directions (Figure 7g). Further increase in film thickness only slightly decreased the N<sub>it</sub> which slightly increased again in the thickest film. This analysis suggests monolayer films exhibited higher charge trap density which may explain its lower hole mobility and higher threshold voltage relative to thicker films. This observation is consistent with the morphological features of monolayers possessing more twisted backbone conformation.

On a side note, we observed the emergence of electron mobility and ambipolar transport characteristic above the critical thickness 27 nm (Figure 7c). At the same time, the on/ off ratio peaked at 27 nm and lowered beyond this thickness (Figure S25, Supporting Information), due to increased off-current with the presence of both charge carrier types in thicker films. Such slight shift from unipolarity to ambipolarity may be related to appearance of face-on crystallites (Figure 5c) that facilitated electron injection.

#### 2.7. Generality of Method for Printing 2D Monolayers

To further demonstrate the generality of using dynamic-templateassisted MGC to fabricate highly ordered 2D monolayer films of semiconducting polymers, we chose another isoindigo-based donor-acceptor conjugated polymer, PII-2T. Indeed, smooth 2D films of PII-2T with thickness of around ≈3.0 nm was obtained on IL using 1 mg mL<sup>-1</sup> chlorobenzene solution at 0.5 mm s<sup>-1</sup> coating speed and 87 °C stage temperature (Figure 8a). The obtained thickness is very close to the out-of-plane lamella stacking distance (2.6 nm) determined using GIXD of multilayer PII-2T films (Figure S26, Supporting Information). We note that the distance between the alkyl-side chain ends in perfectly edge-on PII-2T

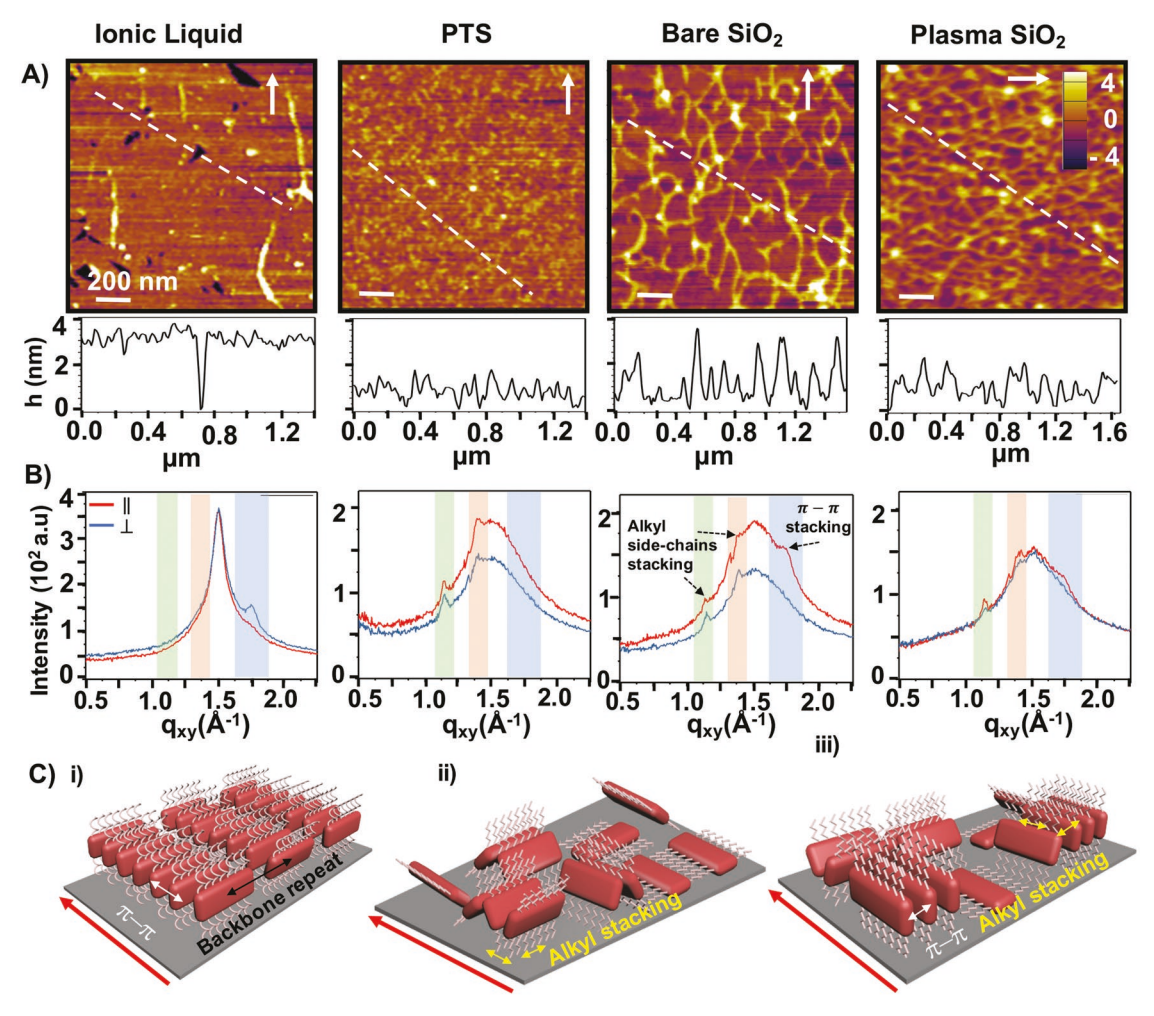


Figure 8. Morphology and molecular packing of PII-2T monolayer films on IL and reference substrates. a) Tapping-mode AFM height images of PII-2T monolayer films printed on IL, PTS, bare SiO2 and plasma treated SiO2 accompanied with the height profile (shown by white dotted lines in the AFM images). b) 1D-GIXD profile of monolayer PII-2T films comparing various substrates with the incident beam parallel (red) and perpendicular (blue) to the coating direction. The curves are obtained by azimuthal integration of radial slices from 2D GIXD pattern (Figure S28, Supporting Information), along in-plane direction (azimuthal angle of  $-83^{\circ}$  to  $-88^{\circ}$ ). The green and orange shaded regions highlight peaks at  $q_{xy} = 1.14$  and 1.40 Å<sup>-1</sup>. These peaks possibly arise from alkyl side-chains stacking. The blue shaded region highlights the  $\pi-\pi$  stacking peak. The strong peak at  $q_w \approx 1.5 \text{ Å}^{-1}$  is due to OTS. c) Molecular stacking model of PII-2T films printed on i) IL ii) PTS and iii) bare and plasma treated SiO<sub>2</sub>.

ADVANCED FUNCTIONAL MATERIALS

determined through Mercury<sup>[14]</sup> is  $\approx 3.3$  nm which also suggests edge-on orientation and possible interdigitation of side-chains in thicker films of PII-2T (Figure S27, Supporting Information). In contrast to IL printed PII-2T monolayer films, bare and plasma treated SiO<sub>2</sub> produced 1D fiber network like morphology in monolayer PII-2T films, with area average of merely 20% and 44% respectively. The films on PTS were instead noncontinuous, comprised of islands of short nanofibers throughout the film.

The molecular packing of IL-templated PII-2T monolayer was similar to that of DPP2T-TT with strong  $\pi$ - $\pi$  stacking peak observed at  $q_{xy} \approx 1.75 \text{ Å}^{-1}$  perpendicular to the coating direction (Figure 8b and Figure S28, Supporting Information). This also suggested edge-on orientation of the polymer with the backbone oriented perpendicular to the coating direction (Figure 8ci). The monolayer coated on PTS did not exhibit  $\pi$ - $\pi$  peak in neither direction, instead weak alkyl side-chains stacking peaks were observed in both directions at  $q_{xy} \approx 1.14$ and 1.40 Å<sup>-1</sup>; this indicates that PTS encourages stacking of alkyl side-chains (Figure 8c-ii) instead of polymer backbone. In contrast, both plasma-treated and bare SiO<sub>2</sub> produced monolayers with weak  $\pi$ - $\pi$  stacking peaks but along the printing direction, opposed to the case of IL (Figure 8c-iii). The monolayers on these substrates also had weak alkyl side-chains stacking peaks in both directions. The proposed models for molecular packing are illustrated in Figure 8c. In addition, we printed PII-2T monolayer films using ink solution in chloroform to test the robustness of our technique with regards to the solvent used (Figure S29, Supporting Information). Indeed, we observed similar morphology and molecular ordering in monolayer films printed using chloroform as that observed using chlorobenzene in IL as well as solid reference substrates.

#### 2.8. Thickness Dependent Sensitivity to Gaseous Biomarker

Finally, we also fabricated OFET based ammonia sensors incorporating DPP2T-TT films of various thicknesses. Ammonia is one of the breath metabolites that could be used as biomarker for renal failure-a disease that is normally diagnosed at a late stage. [27] Highly sensitive OFET based sensors could be utilized as a fast, inexpensive and noninvasive alternative for early diagnosis of the disease through detection of breath ammonia at extremely low concentration. [28] As the gaseous

analyte approaches and diffuses into the OSC film, we expect a first-order charge-transfer reaction to occur between DPP2T-TT and ammonia as follows, where the electron transferred from ammonia reduces the hole concentration in the channel and thereby decreases the current<sup>[29]</sup>

$$DPP2T - TT^{+} \stackrel{\cdots}{N} H_{3} \leftrightarrow DPP2TTT \cdot NH_{3}^{+}$$
(3)

To measure the OFET device sensitivity to ammonia at 1ppb, we covered a single transistor device using a polydimethylsiloxane (PDMS) microfluidic enclosure with an inlet and outlet (**Figure 9a**). Using a two-syringe push–pull pump, 1 mL of ammonia vapor of 1 ppb concentration diluted with nitrogen, was exposed to the OFET device at 10 mL min<sup>-1</sup> flow rate and the resulting current change was recorded. The device sensitivity was defined as

$$S = \frac{I_o - I_g}{I_o} \times 100\% \tag{4}$$

where  $I_{\rm o}$  and  $I_{\rm g}$  refers to the current before and after the gas exposure, respectively. We observed a striking 83% decrease in current when ≈7 nm DPP2T-TT film was exposed to ammonia vapors (Figure 9b). We note that because of the low performance of the monolayer films, we avoided using it in the sensing experiments. As the film thickness increased, the value of S gradually reduced, reaching about ≈42% for 61 nm film. In thicker films, the ammonia vapors need to diffuse through the entire film thickness so as to reach the conductive channel and to react with the hole carriers. Since not all ammonia molecules exposed through the top surface reaches the channel to result in this charge-transfer reaction, the sensitivity declines in thicker films. We observed that the decreased current did not rise back to the original value once it was exposed to ammonia, even after purging the film with nitrogen, which we suspect is due to strong interaction and enhanced binding of the ammonia molecules with DPP2T-TT polymer.

## 3. Conclusion

In this work, we demonstrated dynamic-template-assisted meniscus-guided coating as a new technique to fabricate 2D

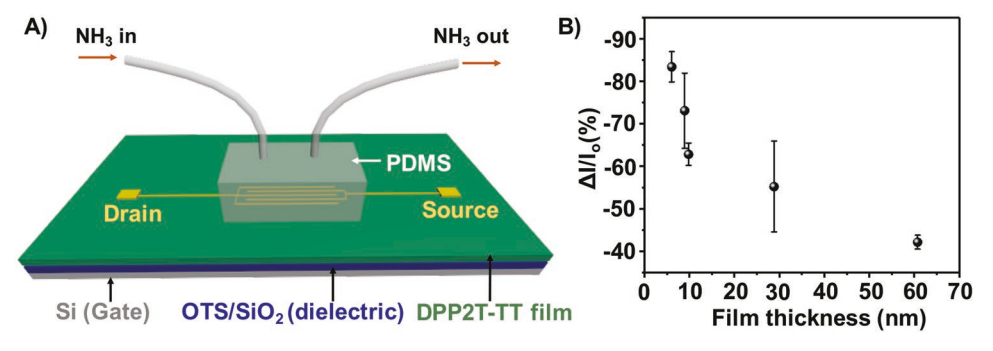


Figure 9. OFET based ammonia sensor incorporating ultrathin DPP2T-TT films. a) Schematic illustration of ammonia sensing setup. The DPP2T-TT films printed on IL and transferred to  $OTS/SiO_2$  are decorated with thermally evaporated  $MoO_3/Ag$  electrode. The area of the substrate-film-electrode ensemble are enclosed in a PDMS chamber with inlet and outlet for ammonia gas with dry nitrogen as the carrier gas. b) Sensitivity of OFET device in (a) with varying thickness of DPP2T-TT to 1 ppb ammonia.



www.afm-journal.de

monolayer films of two donor-acceptor conjugated polymers-DPP2T-TT and PII-2T over centimeter scale. The surface reconfigurability of dynamic template and its strong interaction with conjugated polymers, in synergy with unidirectional flow-guided crystal growth resulted in highly ordered monolayer films with edge-on orientation and polymer backbone aligned perpendicular to printing. In contrast, the reference solid substrates-PTS and plasma treated SiO2 resulted in monolayer films with 1D fiber network morphology riddled with voids. Moreover, these substrates also seem to favor stacking of the alkyl side-chains rather than conjugated backbone, resulting no  $\pi$ - $\pi$  stacking between polymer chains in most of the cases. We also fabricated DPP2T-TT films of various thicknesses using IL and probed into the molecular packing, electronic structure, and electronic properties of 2D monolayers. We observed that the polymer changed from edge-on orientation to bimodal orientation when the film reaches ≈20 nm. This change in molecular ordering was accompanied by a sudden change in electronic structure characterized by abrupt increase in J-aggregation, absorption coefficient and decrease in optical bandgap and HOMO level until similar critical thickness, which we attributed to planarization of DPP2T-TT polymer chains with increase in thickness. This phenomenon was observed irrespective of the substrate used. Moreover, the hole mobility of DPP2T-TT films also followed the exact same trend with thickness, which further strengthened our claim that the DPP2T-TT backbone is more twisted in the monolayer but it rapidly becomes planarized with addition of more layers until a critical thickness. Increasing the film thickness beyond this critical thickness results in twisting of the polymer backbone again and deteriorates the polymer alignment, possibly due to uncontrolled bulk and top surface crystallization occurring far from the substrate.

#### 4. Experimental Section

OSC Film Fabrication: Two donor-acceptor conjugated polymers DPP2T-TT  $(M_n = 42 \ 911 \ \text{g mol}^{-1}, \ M_w = 101 \ 824 \ \text{g mol}^{-1})$  and PII2T  $(M_n = 225 616 \text{ g mol}^{-1}, M_w = 760 326 \text{ g mol}^{-1})$  were synthesized as previously described. The solutions of DPP2T-TT and PII-2T were prepared in chloroform and chlorobenzene (99.8% ACS-grade, Sigma Aldrich), respectively. To prepare the dynamic template substrate, anodized aluminum oxide (AAO) membrane with pore size of 200 nm, 13 mm in diameter (Sigma-Aldrich) was placed in a glass substrate and infiltrated with 1-ethyl-3-methylimidazolium bis(trifluoromethylsulfonyl)imide (EMIM-TFSI) (solvionic, ≥98%) to form an IL/AAO hybrid substrate. Film deposition of the polymer was carried out by sandwiching small volume of ink solution (5-8 μL) between moving OTS-functionalized blade and stationary substrate. The blade front was separated from the substrate by 100 µm and was tilted by  $8^{\circ}$ . The substrate temperature was set at 25 and 87 °C for printing DPP2T-TT/chloroform and PII2T/chlorobenzene solution, respectively. To vary the film thickness, the concentration of the ink solution was changed from 0.5 to 15 mg  $mL^{-1}$  so that the evaporation rate can be maintained constant. During coating of films, the blade was linearly translated at coating speed of 0.5 mm s<sup>-1</sup>, unless specified otherwise. After films were printed on IL/AAO substrates, they were transferred to OTS-functionalized silicon wafer with 300 nm thermally grown SiO<sub>2</sub> by bringing the substrate in close contact with the film/IL/AAO; the film transfer was assisted by dropping 100 µL of ethylene glycol on AAO. The transferred films were then washed with acetonitrile and immersed in the same solvent for at least 30 min to remove the residual IL. For OTS functionalization of the substrate and blade, precleaned SiO<sub>2</sub> wafer with 300 nm oxide layer was first plasma treated and immersed in trichloroethylene solution of OTS (0.2 vol%) at room temperature for 20 min. The wafer was then rinsed with toluene and isopropanol followed by baking at 120 °C for 20 min and finally performing ultrasonication in toluene for 3 min. For PTS functionalization, a precleaned  $\rm SiO_2$  wafer with 300 nm oxide layer was first plasma treated and let to react in a sealed container with 1.5 mL of PTS and 50 mL of anhydrous toluene at 90 °C for 12 h. Then the wafer was washed with toluene followed by ultrasonication in toluene bath for 3 min.

Film Characterization: For all characterization, the polymer films printed on IL/AAO hybrid substrates were transferred to OTS-treated substrates.

Film Morphology and Thickness: The large area morphology of the solution printed OSC films were visualized using optical microscope (Nikon Eclipse CiPOL) and imaging software (NIS-Elements). The films were also visualized under cross-polarized light to observe birefringence. Thickness measurement and mesoscale morphology visualization of the films were performed using an Asylum Cypher AFM with Tap300AI-G tapping mode AFM tips.

Grazing Incidence X-ray Diffraction: GIXD of the films was executed at beamline 8-ID-E of Advanced Photon Source at Argonne National Laboratory.[31] Incident beam energy of 10.92 keV was used to collect the diffraction data on a 2D detector (PILATUS 1M) at two different positions with sample-to-detector distance of 228.165 mm. Samples were scanned with exposure time of 30s under vacuum environment with incidence angle of 0.14°. The images obtained were combined to eliminate most of the inactive pixels using the GIXSGUI package written for MATLAB and further data analysis was performed using the same software.[32] The in-plane peaks and out-of-plane peaks were obtained by azimuthal integration of radial slices with azimuthal range of  $-88^{\circ} < \chi < -83^{\circ}$ and  $-14^{\circ} < \chi < -9^{\circ}$ , respectively, from the geometrically corrected image. Using the same package, corrections were made for detector nonuniformity, beam polarization, and detector sensitivity, and the 2D data were reshaped into the representation  $q_z$  versus  $q_r (= \sqrt{q_x^2 + q_y^2})$ . Multipeak fitting was performed to deconvolute the  $\pi$ - $\pi$  stacking peak from OTS peak, amorphous ring and SiO<sub>2</sub> scattering.

*UV-Vis Spectroscopy*: Polarized ultraviolet-visible absorption spectra of the DPP2T-TT films were recorded at room using Agilent Cary 60 UV-vis spectrophotometer. The incident light was polarized vertically by a broadband thin film polarizer and the scans were taken from 200 to 1100 nm wavelength. The vibrionic peak positions were determined by performing careful multipeak fitting. The optical bandgap was determined by plotting Tauc plot from the UV-vis spectra. To measure the absorption coefficient, the absorption spectra of each film was averaged over multiple in-plane rotation angles.

Cyclic Voltammetry: CV experiments were performed with a CHI760E (CH Instruments) potentiostat, where all electrochemical measurements were conducted inside an Ar-filled glovebox (VTI) environment with  $\rm O_2$  and  $\rm H_2O < 0.1$  ppm. All voltammetric measurements were taken using a standard three-electrode configuration, a Pt wire as counter electrode, a Ag wire as a reference electrode, and the printed films on indium tin oxide (ITO) printed with OTS monolayer as the working electrode. Printed films were assembled in a cell exposing a 7.07 mm² area of the sample. The sample cell was filled with a solution of 0.1 m tetrabutylammonium hexafluorophosphate (TBAPF6) in acetonitrile. Potentials are referenced versus ferrocene redox (FC/FC+), which was used as an internal standard. The HOMO energy level was determined by the following equation

$$HOMO (in eV) = -e(E_{onset,ox} + (-E_{Fc}))$$
(5)

assuming Fc/Fc<sup>+</sup>  $E^{\circ} = -4.80$  eV relative to vacuum.<sup>[33]</sup>

Device Fabrication and Electrical Characterization: Organic field-effect transistor devices of DPP2T-TT films of various thickness were fabricated with bottom-gate, top-contact configuration on highly n-doped Si as gate with 300 nm SiO<sub>2</sub> layer as dielectric. The dielectric consisted of a self-assembled monolayer of OTS in the case of films fabricated using IL. The source and drain electrodes consisted of 7 nm MoO<sub>3</sub> and 35 nm of silver

transfer curves by the equation

www.afm-journal.de

thermally evaporated onto the polymer films through a shadow mask using Kurt J. Lesker Thermal evaporator (Nano 36). The channel length Nanoscale 2011, 3, 20. (L) and width (W) of the OFET devices were 40 and 800 µm, respectively. All of the electrical measurements were performed under nitrogen environment using a Keysight B1500A semiconductor parameter analyzer.

$$I_{DS} = \frac{WC_{i}\mu}{2I} (V_{G} - V_{T})^{2}$$
 (6)

The field-effect mobilities were calculated from the saturated region of

Here, the  $I_{DS}$  is the drain–source current,  $C_i$  is the capacitance of the dielectric (11 nF cm $^{-2}$  for 300 nm SiO<sub>2</sub> dielectric),  $V_G$  is the gate voltage,  $\mu$  is the apparent mobility, and  $V_T$  is the threshold voltage, and W and L are the channel width and length of the device, respectively.

Sensing: An enclosure for OFET device with an inlet and outlet on top was prepared using PDMS to be used as a gas chamber. This microfluidic enclosure with a size of  $3 \times 2 \times 2$  mm<sup>2</sup> was laminated over OFET device of 4400 um and 65 µm channel width and length, respectively. A twosyringe push-pull pump (LongerPump) was connected to a syringe filled with ammonia of 1 ppb concentration. This syringe and a second syringe filled with nitrogen gas were connected with a valve to serve as its inlet. The outlet of the valve was connected to an inlet in the PDMS chamber using a polytetrafluoethylene tubing. 1 mL nitrogen-diluted ammonia vapor at 1 ppb concentration was exposed to the OFET device using the pump with constant flow rate of 10 mL min<sup>-1</sup> and sensing performance was measured using Keysight B1500A.

# **Supporting Information**

Supporting Information is available from the Wiley Online Library or from the author.

## Acknowledgements

This research was primarily supported by the NSF MRSEC: Illinois Materials Research Center under grant number DMR 17-20633. P.K. acknowledges partial support from American Association of University Women (AAUW) International fellowship. Y.D. and K.-Y. H. were partially supported by NSF CAREER award under grant number NSF DMR 18-47828. Y.D. acknowledges partial support from JITRI International Fellowship. Part of the experiments of this research was conducted in Frederick Seitz Materials Research Laboratory Center Facilities, University of Illinois. This research used facilities of the Advanced Photon Source, a U.S Department of Energy (DOE) Office of Science User Facility operated for the DOE Office of Science by Argonne National Laboratory under Contrast No. DE-AC02-06CH11357. The authors are grateful to beamline scientist Joseph W. Strazalka of Advanced Photon Source, Argonne National Laboratory for facilitating the GIXD measurements.

#### **Conflict of Interest**

The authors declare no conflict of interest.

#### **Keywords**

2D, conjugated polymers, dynamic template, monolayers, morphology, organic electronics, printing, transistors

> Received: November 23, 2019 Revised: January 6, 2020 Published online:

- [1] R. Mas-Balleste, C. Gomez-Navarro, J. Gomez-Herrero, F. Zamora,
- [2] a) C. L. Tan, X. H. Cao, X. J. Wu, Q. Y. He, J. Yang, X. Zhang, J. Z. Chen, W. Zhao, S. K. Han, G. H. Nam, M. Sindoro, H. Zhang, Chem. Rev. 2017, 117, 6225; b) K. S. Novoselov, A. Mishchenko, A. Carvalho, A. H. C. Neto, Science 2016, 353, aac9439; c) F. X. Yang, S. S. Cheng, X. T. Zhang, X. C. Ren, R. J. Li, H. L. Dong, W. P. Hu, Adv. Mater. 2018, 30, 1702415.
- [3] a) M. M. Li, D. K. Mangalore, J. B. Zhao, J. H. Carpenter, H. P. Yan, H. Ade, H. Yan, K. Mullen, P. W. M. Blom, W. Pisula, D. M. de Leeuw, K. Asadi, Nat. Commun. 2018, 9, 451; b) F. Ge, S. Y. Wei, Z. Liu, G. H. Wang, X. H. Wang, G. B. Zhang, H. B. Lu, K. Cho, L. Z. Qiu, ACS Appl. Mater. Interfaces 2018, 10, 9602; c) Z. F. Yao, Y. Q. Zheng, Q. Y. Li, T. Lei, S. Zhang, L. Zou, H. Y. Liu, J. H. Dou, Y. Lu, J. Y. Wang, X. D. Gu, J. Pei, Adv. Mater. 2019, 31, 1806747; d) S. F. Yang, X. Zhang, P. L. Chen, Z. T. Liu, J. W. Tian, G. X. Zhang, D. Q. Zhang, Adv. Electron. Mater. 2017, 3, 1700120; e) L. Janasz, M. Gradzka, D. Chlebosz, W. Zajaczkowski, T. Marszalek, A. Kiersnowski, J. Ulanski, W. Pisula, Langmuir 2017, 33, 4189; f) S. Bonacchi, M. Gobbi, L. Ferlauto, M. A. Stoeckel, F. Liscio, S. Milita, E. Orgiu, P. Samori, ACS Nano 2017, 11, 2000; g) S. G. Bucella, A. Luzio, E. Gann, L. Thomsen, C. R. McNeill, G. Pace, A. Perinot, Z. H. Chen, A. Facchetti, M. Caironi, Nat. Commun. 2015, 6, 8394; h) F. J. Zhang, C. A. Di, N. Berdunov, Y. Y. Hu, Y. B. Hu, X. K. Gao, Q. Meng, H. Sirringhaus, D. B. Zhu, Adv. Mater. 2013, 25, 1401; i) Y. Guo, L. Jiang, X. J. Ma, W. P. Hu, Z. H. Su, Polym. Chem. 2013, 4, 4308; j) B. Park, A. Aiyar, J. I. Hong, E. Reichmanis, ACS Appl. Mater. Interfaces 2011, 3, 1574; k) S. Fabiano, C. Musumeci, Z. H. Chen, A. Scandurra, H. Wang, Y. L. Loo, A. Facchetti, B. Pignataro, Adv. Mater. 2012, 24, 951; I) S. Wang, A. Kiersnowski, W. Pisula, K. Mullen, J. Am. Chem. Soc. 2012, 134, 4015; m) J. C. Scott, J. D. J. Samuel, J. H. Hou, C. T. Rettner, R. D. Miller, Nano Lett.. 2006, 6, 2916; n) H. G. O. Sandberg, G. L. Frey, M. N. Shkunov, H. Sirringhaus, R. H. Friend, M. M. Nielsen, C. Kumpf, Langmuir 2002, 18, 10176; o) G. F. Xu, Z. A. Bao, J. T. Groves, Langmuir 2000, 16, 1834; p) J. Paloheimo, P. Kuivalainen, H. Stubb, E. Vuorimaa, P. Ylilahti, Appl. Phys. Lett. 1990, 56, 1157.
- [4] A. Sharma, F. W. A. van Oost, M. Kemerink, P. A. Bobbert, Phys. Rev. B 2012, 85, 235302.
- [5] a) T. Yokota, T. Kajitani, R. Shidachi, T. Tokuhara, M. Kaltenbrunner, Y. Shoji, F. Ishiwari, T. Sekitani, T. Fukushima, T. Someya, Nat. Nanotechnol. 2018, 13, 139; b) S. Arai, S. Inoue, T. Hamai, R. Kumai, T. Hasegawa, Adv. Mater. 2018, 30, 1707256.
- [6] M. M. Li, F. Hinkel, K. Mullen, W. Pisula, Nanoscale 2016, 8, 9211
- [7] a) Z. X. Xu, V. A. L. Roy, Chin. Phys. B 2014, 23, 048501; b) S. Samitsu, T. Shimomura, S. Heike, T. Hashizume, K. Ito, Macromolecules 2010, 43, 7891.
- [8] D. T. Duong, V. Ho, Z. R. Shang, S. Mollinger, S. C. B. Mannsfeld, J. Dacuna, M. F. Toney, R. Segalman, A. Salleo, Adv. Funct. Mater. 2014, 24, 4515.
- [9] E. Mohammadi, C. K. Zhao, Y. F. Meng, G. Qu, F. J. Zhang, X. K. Zhao, J. G. Mei, J. M. Zuo, D. Shukla, Y. Diao, Nat. Commun. **2017**, *8*, 16070.
- [10] a) H. A. Becerril, M. E. Roberts, Z. H. Liu, J. Locklin, Z. N. Bao, Adv. Mater. 2008, 20, 2588; b) G. Giri, E. Verploegen, S. C. B. Mannsfeld, S. Atahan-Evrenk, D. H. Kim, S. Y. Lee, H. A. Becerril, A. Aspuru-Guzik, M. F. Toney, Z. A. Bao, Nature 2011, 480, 504; c) Y. Diao, L. Shaw, Z. A. Bao, S. C. B. Mannsfeld, Energy Environ. Sci. 2014, 7, 2145.
- [11] X. D. Gu, L. Shaw, K. Gu, M. F. Toney, Z. N. Bao, Nat. Commun. **2018**, 9, 534.
- [12] B. B. Patel, Y. Diao, Nanotechnology 2018, 29, 044004.
- [13] F. J. Zhang, E. Mohammadi, X. Y. Luo, J. Strzalka, J. G. Mei, Y. Diao, Langmuir 2018, 34, 1109.



Adv. Funct. Mater. 2020, 1909787

www.advancedsciencenews.com



- [14] C. F. Macrae, P. R. Edgington, P. McCabe, E. Pidcock, G. P. Shields, R. Taylor, M. Towler, J. van De Streek, J. Appl. Crystallogr. 2006, 39, 453
- [15] M. Le Berre, Y. Chen, D. Baigl, Langmuir 2009, 25, 2554.
- [16] F. Doumenc, B. Guerrier, Langmuir 2010, 26, 13959.
- [17] a) G. Qu, J. J. Kwok, E. Mohammadi, F. J. Zhang, Y. Diao, ACS Appl. Mater. Interfaces 2018, 10, 40692; b) C. T. da Rocha, G. Qu, X. G. Yang, R. Shivhare, M. Hambsch, Y. Diao, S. C. B. Mannsfeld, ACS Appl. Mater. Interfaces 2019, 11, 30079.
- [18] W. K. Zhu, E. Mohammadi, Y. Diao, J. Polym. Sci., Part B: Polym. Phys. 2019, 57, 1622.
- [19] H. S. Lee, D. H. Kim, J. H. Cho, M. Hwang, Y. Jang, K. Cho, J. Am. Chem. Soc. 2008, 130, 10556.
- [20] a) M. Gruber, S. H. Jung, S. Schott, D. Venkateshvaran, A. J. Kronemeijer, J. W. Andreasen, C. R. McNeill, W. W. H. Wong, M. Shahid, M. Heeney, J. K. Lee, H. Sirringhaus, *Chem. Sci.* 2015, 6, 6949; b) X. R. Zhang, L. J. Richter, D. M. DeLongchamp, R. J. Kline, M. R. Hammond, I. McCulloch, M. Heeney, R. S. Ashraf, J. N. Smith, T. D. Anthopoulos, B. Schroeder, Y. H. Geerts, D. A. Fischer, M. F. Toney, *J. Am. Chem. Soc.* 2011, 133, 15073.
- [21] M. S. Vezie, S. Few, I. Meager, G. Pieridou, B. Dorling, R. S. Ashraf, A. R. Goni, H. Bronstein, I. McCulloch, S. C. Hayes, M. Campoy-Quiles, J. Nelson, *Nat. Mater.* 2016, 15, 746.
- [22] a) F. C. Spano, C. Silva, Annu. Rev. Phys. Chem. 2014, 65, 477;
  b) K. S. Park, J. J. Kwok, R. Dilmurat, G. Qu, P. Kafle, X. Y. Luo,
  S. H. Jung, Y. Olivier, J. K. Lee, J. G. Mei, D. Beljonne, Y. Diao, Sci. Adv. 2019, 5, eaaw7757.

- [23] T. Eder, T. Stangl, M. Gmelch, K. Remmerssen, D. Laux, S. Hoger, J. M. Lupton, J. Vogelsang, *Nat. Commun.* 2017, 8, 1641.
- [24] M. Marcus, O. R. Tozer, W. Barford, J. Chem. Phys. 164102, 2014, 141, 164101.
- [25] Y. H. Wijsboom, A. Patra, S. S. Zade, Y. Sheynin, M. Li, L. L. W. Shimon, M. Bendikov, Angew. Chem., Int. Ed. 2009, 48, 5443.
- [26] a) M. R. Niazi, R. P. Li, E. Q. Li, A. R. Kirmani, M. Abdelsamie, Q. X. Wang, W. Y. Pan, M. M. Payne, J. E. Anthony, D. M. Smilgies, S. T. Thoroddsen, E. P. Giannelis, A. Amassian, *Nat. Commun.* 2015, 6, 8598; b) W. L. Kalb, B. Batlogg, *Phys. Rev. B* 2010, 81, 035327.
- [27] B. Buszewski, M. Kesy, T. Ligor, A. Amann, Biomed. Chromatogr. 2007, 21, 553.
- [28] G. Konvalina, H. Haick, Acc. Chem. Res. 2014, 47, 66.
- [29] F. J. Zhang, G. Qu, E. Mohammadi, J. G. Mei, Y. Diao, Adv. Funct. Mater. 2017, 27, 1701117.
- [30] a) Z. Y. Chen, M. J. Lee, R. S. Ashraf, Y. Gu, S. Albert-Seifried, M. M. Nielsen, B. Schroeder, T. D. Anthopoulos, M. Heeney, I. McCulloch, H. Sirringhaus, Adv. Mater. 2012, 24, 647; b) T. Lei, J. H. Dou, J. Pei, Adv. Mater. 2012, 24, 6457.
- [31] Z. Jiang, X. F. Li, J. Strzalka, M. Sprung, T. Sun, A. R. Sandy, S. Narayanan, D. R. Lee, J. Wang, J. Synchrotron Radiat. 2012, 19, 627.
- [32] Z. Jiang, J. Appl. Crystallogr. 2015, 48, 917.
- [33] J. Pommerehne, H. Vestweber, W. Guss, R. F. Mahrt, H. Bassler, M. Porsch, J. Daub, Adv. Mater. 1995, 7, 551.